

Field dependence of the vortex structure in chiral p -wave superconductors

Masanori Ichioka* and Kazushige Machida†

Department of Physics, Okayama University, Okayama 700-8530, Japan

(Dated: February 28, 2002)

To investigate the different vortex structure between two chiral pairing $p_x \pm ip_y$, we calculate the pair potential, the internal field, the local density of states, and free energy in the vortex lattice state based on the quasiclassical Eilenberger theory, and analyze the magnetic field dependence. The induced opposite chiral component of the pair potential plays an important role in the vortex structure. It also produces \sqrt{H} -behavior of the zero-energy density of states at higher field. These results are helpful when we understand the vortex states in Sr_2RuO_4 .

PACS numbers: 74.60.Ec, 74.20.Rp, 74.70.Pq, 74.25.Jb

I. INTRODUCTION

For the superconducting state in quasi-two-dimensional metal Sr_2RuO_4 , the pairing symmetry is suggested to be the chiral p -wave pairing with the basic form $\Delta_{\pm} \sim p_x \pm ip_y$ and inplane equal-spin pairing.^{1,2} For the experimental evidence, the spin triplet pairing is supported by the ¹⁷O-NMR measurement, which reported that there is no reduction of the Knight shift in the superconducting state.³ The pairing state with broken time reversal symmetry is claimed by the μSR measurement, which reported that spontaneous magnetic moment is induced in the superconducting state.⁴

Since the Δ_+ state and the Δ_- state are degenerate at zero field, we expect the domain formation of the two states Δ_+ and Δ_- . We call them as the p_+ -wave domain and the p_- -wave domain, respectively. This degeneracy is lifted under external magnetic field perpendicular to the basal plane, since Δ_{\pm} is the broken time reversal symmetry state with an orbital angular momentum along the z -axis. Then, the vortex in the mixed state shows the different structure for the p_+ -wave and the p_- -wave domains. We consider the case when $\mathbf{H} \parallel \hat{z}$ for $e > 0$ ($2e$ is the charge of the Cooper pair) or equivalently when $\mathbf{H} \parallel -\hat{z}$ for $e < 0$. In these cases, there appear winding $+1$ vortices. It is parallel (antiparallel) to the internal winding of the Cooper pair in the p_+ -wave (p_- -wave) domain. The information of the vortex structure for the p_{\pm} -wave domain is important to analyze the chirality p_{\pm} of each domain.

The differences of the vortex structure for the p_+ -wave and the p_- -wave domains have been studied by the two component Ginzburg-Landau (GL) theory,^{5,6} the quasiclassical theory,^{7,8} and the Bogoliubov-de Gennes (BdG) theory.^{6,9,10,11} In the chiral p -wave superconductors, it is important to consider the opposite chiral component Δ_{\mp} which is induced around the vortex of the dominant Δ_{\pm} component in the p_{\pm} -wave domains. This induced component shows different spatial structure for the p_+ -wave and the p_- -wave domains. This is the origin of the different vortex structure. There is a free energy difference between the p_+ -wave and the p_- -wave domain cases in the vortex state, which leads to the different upper criti-

cal field H_{c2} for these chiral states. The estimation of H_{c2} was reported by Scharnberg and Klemm in the isotropic three dimensional Fermi surface case.^{12,13} Following their results, H_{c2} of the p_+ -wave domain, which is noted as ABM state, is near that of the isotropic s -wave pairing case, because the opposite Δ_- -component is not induced along H_{c2} -line. On the other hand, the vortex state in the p_- -wave domain, which is noted as the generalized ABM state or the SK state, gives higher H_{c2} because there is large induced Δ_+ -component. That is, we can say that the superconductivity survives until high field in the p_- -wave domain case by the enhancement due to the induced opposite chiral component. Since the difference of H_{c2} is large (about twice) for these domain cases, it is important to know the H (external magnetic field) dependence of the vortex structure for Δ_+ and Δ_- continuously for all H regions, in order to study the chiral-dependent properties.

In this paper, we investigate the field dependence of the vortex structure for the p_{\pm} -wave domain cases, based on the quasiclassical Eilenberger theory.¹⁴ Our calculation method for the vortex lattice state was established for the study of the $d_{x^2-y^2}$ -wave pairing case in high- T_c superconductors.^{15,16,17,18,19,20} We can calculate both the pair potential and the vector potential selfconsistently. In this paper, we consider the case of small GL parameter $\kappa = 2.7$ appropriate to Sr_2RuO_4 .²¹ In the quasiclassical theory, we can also consider the quasiparticle states around the vortex, such as the local density of states (LDOS). Among them, H -dependence of the spatially averaged zero energy density of states (DOS) $N(0)$ is important. It is accessible by the specific heat measurement. For example, in the $d_{x^2-y^2}$ -wave pairing such as in high T_c superconductors, there is a relation $N(0) \sim \sqrt{H}$ due to the line node of the superconducting gap for $\mathbf{H} \parallel c$.^{22,23,24} It is because low energy quasiparticles propagating to the node direction can extend far from vortex. In the relation $N(0) \sim H^{\alpha}$ in the s -wave pairing case, α can be smaller than 1. It is related to the field dependence of the vortex core radius.^{25,26,27,28,29} These behaviors could be confirmed by the calculation based on the quasiclassical theory.¹⁵ In Sr_2RuO_4 , the specific heat measurement suggests the relation $N(0) \sim \sqrt{H}$ at higher field, giving the discussion on the possibility of

the line node.³⁰ Then, it is important to examine the origin of the \sqrt{H} -behavior.

There are detailed discussions on the pairing function of the chiral p -wave for Sr_2RuO_4 , including the gap anisotropy and the orbital dependence.^{31,32,33,34,35,36,37} But, here, we consider the fundamental case of the simple isotropic gap function $\Delta_{\pm} = (p_x \pm ip_y)/p_F = e^{\pm i\theta}$ on the two-dimensional isotropic Fermi surface $(p_x, p_y) = p_F(\cos\theta, \sin\theta)$ in order to focus on the chirality dependence, without including the anisotropy effect of the superconducting gap or Fermi surfaces.

After describing our formulation of the quasiclassical theory in Sec. II, we evaluate the free energy in Sec. III. The pair potential and internal field structure of the vortex lattice state are studied in Sec. IV. The low energy quasiparticle states are examined in Sec. V by considering the LDOS and the field dependence of the DOS. The last section is devoted to summary and discussions.

II. QUASICLASSICAL EILENBERGER THEORY

Our calculation is performed by extending the quasiclassical method for the vortex lattice state in the $d_{x^2-y^2}$ -wave pairing case^{15,16,17,18,19,20} to the chiral p -wave pairing case. For the details of the calculation method, also see Refs. 38,39,40. We consider the case of the clean limit and cylindrical Fermi surface. First, to obtain the pair potential $\Delta(\theta, \mathbf{r})$ and vector potential $\mathbf{A}(\mathbf{r})$ selfconsistently, we solve the Eilenberger equation in the Matsubara frequency $\omega_n = (2n+1)\pi T$ for the quasiclassical Green's functions $g(i\omega_n, \theta, \mathbf{r})$, $f(i\omega_n, \theta, \mathbf{r})$ and $f^\dagger(i\omega_n, \theta, \mathbf{r})$, where \mathbf{r} is the center of mass coordinate of a Cooper pair. The direction of the relative momentum of the Cooper pair, $\hat{\mathbf{k}} = \mathbf{k}/|\mathbf{k}|$, is denoted by an angle θ measured from the x axis. The Eilenberger equation is given by¹⁴

$$\left\{ \omega_n + \frac{i}{2} \mathbf{v}_F \cdot \left(\frac{\nabla}{i} + \frac{2\pi}{\phi_0} \mathbf{A}(\mathbf{r}) \right) \right\} f(i\omega_n, \theta, \mathbf{r}) = \Delta(\theta, \mathbf{r}) g(i\omega_n, \theta, \mathbf{r}), \quad (1)$$

$$\left\{ \omega_n - \frac{i}{2} \mathbf{v}_F \cdot \left(\frac{\nabla}{i} - \frac{2\pi}{\phi_0} \mathbf{A}(\mathbf{r}) \right) \right\} f^\dagger(i\omega_n, \theta, \mathbf{r}) = \Delta^*(\theta, \mathbf{r}) g(i\omega_n, \theta, \mathbf{r}), \quad (2)$$

$$g(i\omega_n, \theta, \mathbf{r}) = [1 - f(i\omega_n, \theta, \mathbf{r}) f^\dagger(i\omega_n, \theta, \mathbf{r})]^{1/2}, \quad (3)$$

where $\text{Reg}(i\omega_n, \theta, \mathbf{r}) > 0$, the Fermi velocity $\mathbf{v}_F = v_F \hat{\mathbf{k}}$, the flux quantum ϕ_0 and $e = -|e|$. In the symmetric gauge, $\mathbf{A}(\mathbf{r}) = \frac{1}{2} \mathbf{H} \times \mathbf{r} + \mathbf{a}(\mathbf{r})$, where $\mathbf{H} = (0, 0, H)$ is a uniform field and $\mathbf{a}(\mathbf{r})$ is related to the internal field $\mathbf{h}(\mathbf{r}) = (0, 0, h(\mathbf{r}))$ as $\mathbf{h}(\mathbf{r}) = \nabla \times \mathbf{a}(\mathbf{r})$. For the coupling to a magnetic field, we neglect the paramagnetic coupling to the spin, and consider the effect of the orbital coupling in the vector potential terms.

The self-consistent conditions for $\Delta(\theta, \mathbf{r})$ and $\mathbf{a}(\mathbf{r})$ are

given as

$$\Delta(\theta, \mathbf{r}) = N_0 2\pi T \sum_{\omega_n > 0} \int_0^{2\pi} \frac{d\theta'}{2\pi} V(\theta', \theta) f(i\omega_n, \theta', \mathbf{r}), \quad (4)$$

$$\nabla \times \nabla \times \mathbf{a}(\mathbf{r}) = -\frac{\pi\phi_0}{\kappa^2 \Delta_0 \xi_0^3} 2\pi T \sum_{\omega_n > 0} \int_0^{2\pi} \frac{d\theta}{2\pi} \frac{\hat{\mathbf{k}}}{i} g(i\omega_n, \theta, \mathbf{r}), \quad (5)$$

with the pairing interaction $V(\theta', \theta)$ and $\kappa = (7\zeta(3)/72)^{1/2} (\Delta_0/T_c) \kappa_{\text{BCS}}$ with Riemann's zeta function $\zeta(3)$. N_0 is the density of states at the Fermi surface, Δ_0 is the uniform gap at $T = 0$, and κ_{BCS} is the GL parameter in the BCS theory. We set the energy cutoff $\omega_c = 20T_c$ and $\kappa_{\text{BCS}} = 2.7$. In the following, energies and lengths are measured in units of Δ_0 and $\xi_0 = v_F/\Delta_0 = \pi \xi_{\text{BCS}}$ (ξ_{BCS} is the BCS coherence length), respectively. The magnetic fields are measured in units of ϕ_0/ξ_0^2 .

By solving Eqs. (1)-(3) in the so-called explosion method, we estimate the quasiclassical Green's functions at 41×41 discretized points in a unit cell of the vortex lattice. Using the symmetry relation^{18,38} described in Appendix, we can reduce the range of \mathbf{r} and θ in the calculation solving Eqs. (1)-(3). We obtain new $\Delta(\theta, \mathbf{r})$ and $\mathbf{a}(\mathbf{r})$ from Eqs. (4) and (5), and use them at the next step calculation of Eqs. (1)-(3). This iteration procedure is repeated until sufficiently selfconsistent solution is obtained. When we consider the lattice transformation $\mathbf{R} = m\mathbf{r}_1 + n\mathbf{r}_2$ (m, n : integers) with the unit vectors $\mathbf{r}_1 = (a_x, 0)$, $\mathbf{r}_2 = (\zeta a_x, a_y)$ of the vortex lattice and $H a_x a_y = \phi_0$, there is a relation

$$\Delta(\theta, \mathbf{r} + \mathbf{R}) = \Delta(\theta, \mathbf{r}) e^{i\chi(\mathbf{r}, \mathbf{R})}, \quad \mathbf{a}(\mathbf{r} + \mathbf{R}) = \mathbf{a}(\mathbf{r}), \quad (6)$$

where

$$\chi(\mathbf{r}, \mathbf{R}) = -\frac{\pi}{\phi_0} (\mathbf{H} \times \mathbf{R}) \cdot (\mathbf{r} + 2\mathbf{r}_0) - \pi mn \quad (7)$$

in the symmetric gauge. Then, we can know $\Delta(\theta, \mathbf{r})$ and $\mathbf{a}(\mathbf{r})$ in the other region out of the calculated unit cell region. There is a vortex center at $\mathbf{r}_0 = \frac{1}{2}(\mathbf{r}_1 + \mathbf{r}_2)$. When we consider the case when a vortex center locates at $\mathbf{r} = 0$, we set $\mathbf{r}_0 = \frac{1}{2}(\mathbf{r}_1 + \mathbf{r}_2)$. The spatial variation of the internal field and the current $\mathbf{J}(\mathbf{r}) = (c/4\pi)\nabla \times \mathbf{h}(\mathbf{r})$ is calculated from $\mathbf{a}(\mathbf{r})$. The current is scaled by $c\phi_0/4\pi\xi_0$ in figures. To study the field dependence, our calculations are performed for various fields at fixed temperature $T/T_c = 0.5$.

In the chiral p -wave pairing, we can set

$$\Delta(\theta, \mathbf{r}) = \Delta_+(\mathbf{r})\phi_+(\theta) + \Delta_-(\mathbf{r})\phi_-(\theta), \quad (8)$$

$$V(\theta', \theta) = \bar{V}[\phi_+^*(\theta')\phi_+(\theta) + \phi_-^*(\theta')\phi_-(\theta)] \quad (9)$$

with the pairing functions $\phi_{\pm}(\theta) = e^{\pm i\theta}$. For the p_+ -wave domain case, we start our calculations from the initial state $\Delta_+(\mathbf{r}) = \Psi_0(\mathbf{r})$ and $\Delta_-(\mathbf{r}) = 0$ with the vortex lattice solution $\Psi_0(\mathbf{r})$ in the lowest Landau level. In this case, $\Delta_-(\mathbf{r})$ gives the induced component around

the vortex after we obtain selfconsistent results. For the p_- -wave domain case, we start from the initial state $\Delta_-(\mathbf{r}) = \Psi_0(\mathbf{r})$ and $\Delta_+(\mathbf{r}) = 0$.

When we consider the one component case for the pair potential by neglecting the induced component, $\Delta(\theta, \mathbf{r}) = \Delta_+(\mathbf{r})\phi_+(\theta)$ and $\Delta(\theta, \mathbf{r}) = \Delta_-(\mathbf{r})\phi_-(\theta)$ in the p_+ -wave and the p_- -wave domain cases, respectively. In this case, by setting $\phi_\pm(\theta) = |\phi_\pm(\theta)|e^{\pm i\theta}$, $f(i\omega_n, \theta, \mathbf{r}) = \bar{f}(i\omega_n, \theta, \mathbf{r})e^{\pm i\theta}$ and $f^\dagger(i\omega_n, \theta, \mathbf{r}) = \bar{f}^\dagger(i\omega_n, \theta, \mathbf{r})e^{\mp i\theta}$, we can remove the phase factor $e^{\pm i\theta}$ out of the Eilenberger equations. Then, the Eilenberger equations for $\bar{f}(i\omega_n, \theta, \mathbf{r})$ and $\bar{f}^\dagger(i\omega_n, \theta, \mathbf{r})$ are solved under the pair potential $\Delta(\theta, \mathbf{r}) = \Delta_\pm(\mathbf{r})|\phi_\pm(\theta)| = \Delta_\pm(\mathbf{r})$, which is the pair potential for the isotropic s -wave pairing. Then, unless we consider the induced component, the vortex structure is the same as that of the s -wave pairing case, and there are no differences for the p_+ -wave and the p_- -wave domain cases. Therefore, two component pair potential is intrinsic and essential for the vortex structure in the chiral p -wave superconductors. We also calculate the vortex structure in the isotropic s -wave pairing case for reference.

The free energy F is calculated as^{14,16,38}

$$\frac{F}{N_0\Delta_0^2} = \kappa^2 \frac{\langle h(\mathbf{r})^2 \rangle_{\mathbf{r}}}{(\phi_0/\xi_0^2)^2} + \frac{\langle |\Delta_+(\mathbf{r})|^2 + |\Delta_-(\mathbf{r})|^2 \rangle_{\mathbf{r}}}{N_0\bar{V}\Delta_0^2} - \frac{2\pi T}{\Delta_0^2} \sum_{\omega_n > 0} \int_0^{2\pi} \frac{d\theta}{2\pi} \langle I(\omega_n, \theta, \mathbf{r}) \rangle_{\mathbf{r}} \quad (10)$$

with

$$I(\omega_n, \theta, \mathbf{r}) = \Delta^*(\theta, \mathbf{r})f + \Delta(\theta, \mathbf{r})f^\dagger - (1-g) \left[\frac{1}{f} \left\{ \omega_n + \frac{i}{2} \mathbf{v}_F \cdot \left(\frac{\nabla}{i} + \frac{2\pi}{\phi_0} \mathbf{A}(\mathbf{r}) \right) \right\} f + \frac{1}{f^\dagger} \left\{ \omega_n - \frac{i}{2} \mathbf{v}_F \cdot \left(\frac{\nabla}{i} - \frac{2\pi}{\phi_0} \mathbf{A}(\mathbf{r}) \right) \right\} f^\dagger \right] \quad (11)$$

$$= \frac{\Delta^*(\theta, \mathbf{r})f + \Delta(\theta, \mathbf{r})f^\dagger}{1+g}, \quad (12)$$

where g , f and f^\dagger mean $g(i\omega_n, \theta, \mathbf{r})$, $f(i\omega_n, \theta, \mathbf{r})$ and $f^\dagger(i\omega_n, \theta, \mathbf{r})$, respectively. For the spatial average, $\langle \dots \rangle_{\mathbf{r}} = \int_{\text{unit cell}} d\mathbf{r} (\dots) / S$, where S is the area of a unit cell. We use Eqs. (1)-(3) to obtain Eq. (12).

The LDOS for energy E is calculated as

$$N(E, \mathbf{r}) = N_0 \int_0^{2\pi} \frac{d\theta}{2\pi} \text{Re } g(i\omega_n \rightarrow E + i\eta, \theta, \mathbf{r}). \quad (13)$$

To obtain $g(i\omega_n \rightarrow E + i\eta, \theta, \mathbf{r})$, we solve Eqs. (1)-(3) for $\eta - iE$ instead of ω_n using the self-consistently obtained $\Delta(\theta, \mathbf{r})$ and $\mathbf{a}(\mathbf{r})$. We typically use $\eta = 0.01$. The DOS is given by the spatial average of the LDOS as

$$N(E) = \langle N(E, \mathbf{r}) \rangle_{\mathbf{r}}. \quad (14)$$

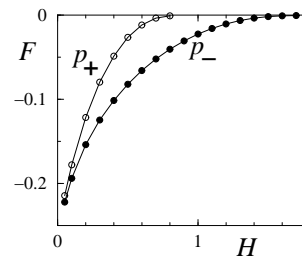


FIG. 1: Free energy as a function of H . We plot $F/(N_0\Delta_0^2)$ for the p_+ -wave domain case (o) and the p_- -wave domain case (●).

III. FREE ENERGY

For the estimation of the free energy difference between the p_+ -wave domain and the p_- -wave domain cases, we show the field dependence of the free energy F in Fig. 1. The p_- -wave domain case has lower free energy than that of the p_+ -wave domain case. Then, the p_- -wave domain is stable, and the p_+ -wave domain may exist as a metastable state. We expect that the transition of the p_+ -wave domain to the p_- -wave domain is stimulated with increasing field, since the free energy difference increases. The upper critical field $H_{c2} \sim 0.81$ in the p_+ -wave domain case, and $H_{c2} \sim 1.7$ in the p_- -wave domain case. Then, the p_+ -wave domain does not exist at $H > 0.81$.

The estimation of the stable vortex lattice configuration is also important, since the vortex lattice may be deformed from the triangular lattice due to the induced opposite chiral component.^{12,13} Since our calculation method needs long computational time, we can not check all possible vortex lattice configurations. Then, we compare the free energy for the triangular and the square lattice configurations, and discuss the stable vortex lattice configuration. The free energy difference is less than 10^{-3} of F . We use finer 121×121 mesh within a unit cell to carefully estimate the difference. For higher field $H > 0.35$, the square lattice configuration has lower free energy than the triangular one. It suggests that the square lattice is stable at higher field in the p_- -wave domain case. This is qualitatively consistent to the analysis by the GL theory, which suggests the square lattice configuration at higher field.^{41,42} And the square lattice is observed by neutron scattering experiment.⁴³ On the other hand, we obtain the result that the free energy of the triangular lattice is lower for all H range in the p_+ -wave domain case. It is because the induced opposite chiral component is small, as discussed later, and the vortex structure is similar to that of the isotropic s -wave pairing case. If the p_- -wave domain and the metastable p_+ -wave domain coexist, we may observe the different vortex lattice configurations for the domains.

In the following subsections, we investigate the origin of the difference of the vortex structure between the p_- -wave domain and the p_+ -wave domains. The vortex

structure is examined both in the square and the triangular vortex lattice configurations. Since our purpose is to find the chirality effect on the vortex structure by comparing the both chirality cases, we mainly report the results in the same situation of the square lattice configuration. The square lattice is expected in the stable p_- -wave domain case. After that, we briefly comment on the triangular lattice configuration case.

IV. VORTEX STRUCTURE

A. Vortex structure in the p_- -wave domain

First, we consider the vortex structure in the p_- -wave domain case. It is shown in Fig. 2 (a) and (b) within a unit cell of the square vortex lattice, i.e., square area in Fig. 3 (a). The profiles are presented along the path V-S-C-V shown in Fig. 3 (a). Line VS is along the nearest neighbor (NN) vortex direction, and line SC is along the boundary of the unit cell. Dashed line VC is along the next nearest neighbor (NNN) vortex direction. The dominant component $|\Delta_-(\mathbf{r})|$ shows a conventional vortex structure. At low field, as shown in Fig. 2(a), $|\Delta_-(\mathbf{r})|$ is recovered to Δ_0 outside of the vortex core. The shape of the vortex core is square-like. At higher field $H = 0.8$ ($\sim 0.5H_{c2}$) shown in Fig. 2(b), $|\Delta_-(\mathbf{r})|$ is not recovered to Δ_0 even in the boundary of the unit cell, since the inter-vortex distance is small. Along the NN vortex direction, $|\Delta_-(\mathbf{r})|$ is slightly suppressed at the boundary region, compared to the NNN vortex direction.

The opposite chiral $\Delta_+(\mathbf{r})$ component is induced around the vortex core. At low field, the induced component is decayed outside of the vortex core. But at higher field, $|\Delta_+(\mathbf{r})|$ has maximum at the S-points on the boundary. The induced component $\Delta_+(\mathbf{r})$ always vanishes at the vortex center and at the C points. At the vortex center (the C points), $|\Delta_+(\mathbf{r})|$ recovers with the r -linear (r^2 -) dependence. These r -dependences are related to the phase winding of $\Delta_+(\mathbf{r})$, which is presented in Fig. 3 (b) schematically. At the vortex center, when the dominant component $\Delta_-(\mathbf{r})$ has $+1(\times 2\pi)$ winding as shown in Fig. 3 (a), the induced $\Delta_+(\mathbf{r})$ component has opposite -1 winding. It is consistent with the results of previous theories.^{5,6,7,8,9,10,11} Since the total of the winding should be $+1$ within a unit cell, $\Delta_+(\mathbf{r})$ has also $+2$ winding at the C-points, i.e., corners of the square unit cell. These winding structures are the same for all H range.

The screening current $|\mathbf{J}(\mathbf{r})|$ has maximum at the scale of the vortex core radius, and it is decreased with approaching the boundary of the unit cell. At the S- and C-points, $|\mathbf{J}(\mathbf{r})| = 0$. By this screening current, the internal field is produced. It has maximum at the vortex center, and it is decreased outside of the core. At low field, $h(\mathbf{r})$ has minimum at C, and monotonically increases toward the S-point along the boundary. But, at high field, $|\mathbf{J}(\mathbf{r})|$ and $h(\mathbf{r})$ show anomalous behaviors at the boundary region. The profile of $h(\mathbf{r})$ has a peak at a point between

the S and the C points along the boundary line.

B. Vortex structure in the p_+ -wave domain

Next, we consider the vortex in the p_+ -wave domain, which is shown in Fig. 2(c) and (d). The vortex core shape of the dominant component shows circular shape at low field, as shown in the contour line of $|\Delta_+(\mathbf{r})|$ in Fig. 2 (c). The induced component $\Delta_-(\mathbf{r})$ becomes zero at the vortex center and the C-points also in this case. The amplitude $|\Delta_-(\mathbf{r})|$ recovers with the r^2 -behavior around the corners C, as in the p_- -wave domain case. But, the recovery at the vortex center shows the r^3 -behavior, instead of the r -linear. It is because $\Delta_-(\mathbf{r})$ has $+3$ winding at the vortex center, as schematically presented in Fig. 3 (c). The winding -2 at the C-point is not changed. Compared with the p_- -wave domain case, internal field $h(\mathbf{r})$ at the vortex core is larger, since $|\mathbf{J}(\mathbf{r})|$ around the vortex is larger.

At high field, the winding structure of the induced component $\Delta_-(\mathbf{r})$ is changed around the vortex center. The $+3$ winding at the vortex center splits to a -1 winding at the center and four $+1$ winding points around the core, as schematically shown in Fig. 3 (d). As is seen in Fig. 2(d), $|\Delta_-(\mathbf{r})| = 0$ at these $+1$ winding points. As for $|\mathbf{J}(\mathbf{r})|$ and $h(\mathbf{r})$, the high field case shows the similar structure as in the low field case, while their strengths are suppressed with increasing field.

C. In the triangular lattice configuration

We briefly report the vortex structure in the triangular vortex lattice configuration. In this case, the winding structure at the corner of the unit cell is changed. In the p_- -wave (p_+ -wave) domain case, $+2$ (-2) winding in the square lattice becomes $+1$ (-1) winding at the corners of the hexagonal unit cell in the triangular lattice, as shown in Fig. 4 (a)-(c). In the square lattice case, the winding structure at the vortex center changes from $+3$ to -1 on raising field in the p_+ -wave domain case [Fig. 3 (c) and (d)], the vortex center keeps $+3$ winding for all H range in the triangular lattice configuration.

As an example, we show the profile of the vortex structure for the p_- -wave domain at $H = 0.8$ in Fig. 4(d), which is plotted along the NN direction (VS line in Fig. 4(a)), boundary line (SC line) and the NNN direction (VC line) in the triangular vortex lattice. Compared with Fig. 2(d) in the square lattice configuration, the recovery of the induced component around the C-points shows r -linear relation instead of the r^2 -behavior, reflecting the change of the winding structure. There appears anomalous field distribution at higher field in the p_- -wave domain. But, its profile is different from that of the square lattice case. In the triangular lattice, $h(\mathbf{r})$ has minimum at the S-points. However, the p_+ -wave domain case and the low field p_- -wave domain case show quali-

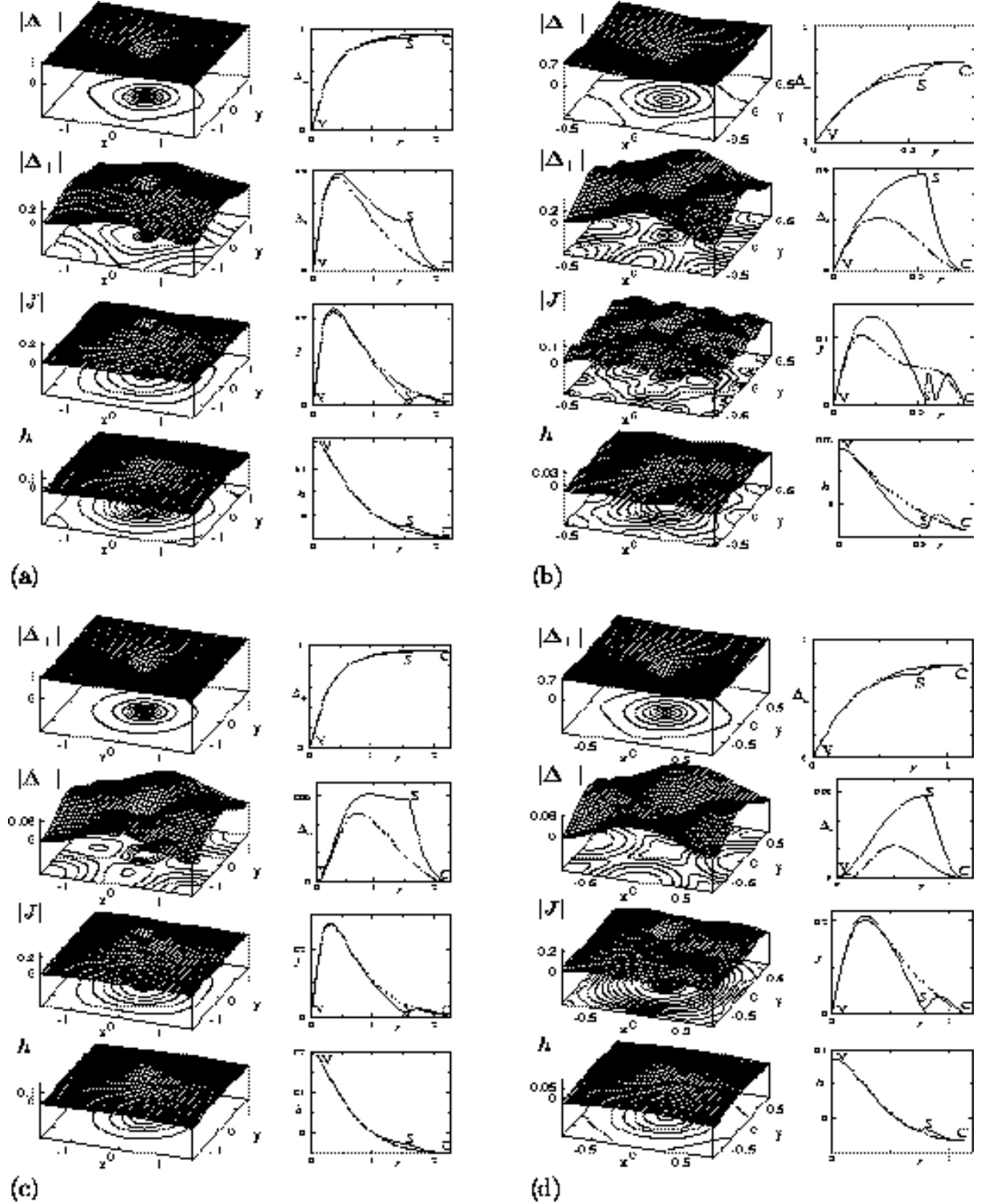


FIG. 2: Vortex structure in the square vortex lattice configuration of the p_- -wave domain case at low field $H = 0.1$ (a) and at high field $H = 0.8$ (b), and in the p_+ -wave domain case at $H = 0.1$ (c) and $H = 0.4$ (d). From upper panels, we plot the dominant pair potential $|\Delta_{\mp}(\mathbf{r})|$, the induced component $|\Delta_{\pm}(\mathbf{r})|$, the screening current $|\mathbf{J}(\mathbf{r})|$, and the internal field $h(\mathbf{r})$, respectively. The left panels are the stereographic view within a unit cell region. There is a vortex at the center of the figures. The right panels are the profiles along the path V-S-C-V presented in Fig. 3(a).

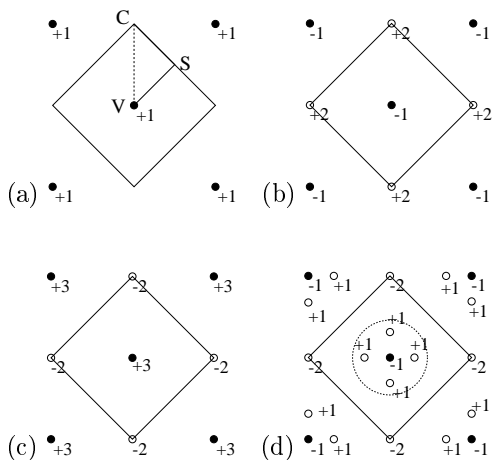


FIG. 3: Phase winding structure of the pair potential in the square vortex lattice configuration. The vortex centers and other singularity points are, respectively, presented by \bullet and \circ . We show the winding number for these points in the figures. The square area means a unit cell of the vortex lattice. (a) The phase of the dominant component. There is a winding $+1(\times 2\pi)$ at the vortex center. Along lines V-S-C-V, we consider profiles of the vortex structure in Fig. 2. (b) The phase of the induced pair potential $\Delta_+(\mathbf{r})$ in the p_- -wave domain case. (c) The phase of the induced pair potential $\Delta_-(\mathbf{r})$ at low field in the p_+ -wave domain case. (d) The same as (c), but at high field. Total winding number is $+3$ within the dotted circle around the vortex core.

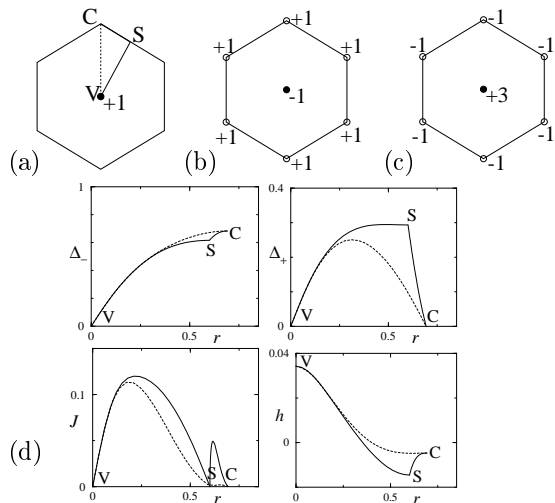


FIG. 4: Phase winding structure in the triangular vortex lattice configuration for the dominant component (a), and the induced component in the p_- -wave domain case (b) and the p_+ -wave domain case (c). The vortex centers and other singularity points are, respectively, presented by \bullet and \circ . We show the winding number for these points in the figures. The hexagonal area means a unit cell of the vortex lattice. (d) The profile of the vortex structure in the triangular vortex lattice configuration of the p_- -wave domain case at high field $H = 0.8$. We plot the dominant pair potential $|\Delta_-(\mathbf{r})|$, the induced component $|\Delta_+(\mathbf{r})|$, the screening current $|\mathbf{J}(\mathbf{r})|$ and the internal field $h(\mathbf{r})$ along the path V-S-C-V presented in (a).

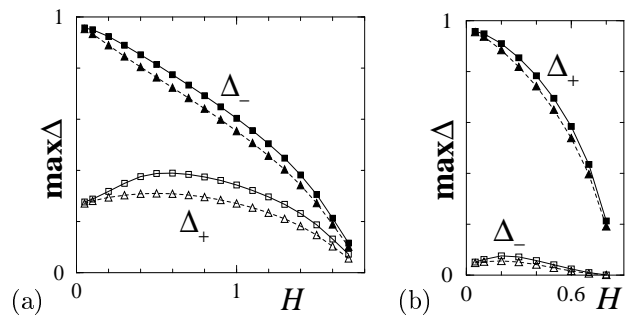


FIG. 5: Field dependence of the amplitude of the dominant and the induced pair potentials in the p_- -wave domain case (a) and in the p_+ -wave domain case (b). We plot $\max|\Delta_-(\mathbf{r})|$ and $\max|\Delta_+(\mathbf{r})|$ as a function of H . Solid (dashed) lines are for the square (triangular) vortex lattice configuration.

tatively the same field distribution as that of the square lattice case in the profile plot. There, $h(\mathbf{r})$ has minimum at the C points.

D. Magnetic field dependence

In this subsection, we investigate the continuous field dependence of the vortex structure. The field dependence of $\Delta_-^{\max} = \max|\Delta_-(\mathbf{r})|$ and $\Delta_+^{\max} = \max|\Delta_+(\mathbf{r})|$ is presented in Fig. 5. We show it both for the square lattice and the triangular lattice configurations. In the p_- -wave domain case, the induced Δ_+^{\max} is large. When the amplitude of the dominant Δ_-^{\max} is decreased with raising field, the ratio of the induced component, $\Delta_+^{\max}/\Delta_-^{\max}$, increases monotonically up to H_{c2} . Due to this large induced component, the superconductivity in the p_- -wave domain case can survive until higher magnetic field, giving high H_{c2} .

On the other hand, in the p_+ -wave domain case, the induced component Δ_-^{\max} is small. The ratio of the induced component, $\Delta_-^{\max}/\Delta_+^{\max}$, decreases as a function of H at higher field, after increasing at low field. Since the ratio is reduced to zero at $H \rightarrow H_{c2}$, the p_+ -wave domain has the same H_{c2} as in the isotropic s -wave pairing in the two dimensional Fermi surface case. We also calculate the isotropic s -wave case, which is equivalent to the case when we neglect the induced component of the chiral p -wave case. The field dependence of $\max|\Delta(\mathbf{r})|$ in the s -wave pairing is almost the same as that of Δ_+^{\max} in Fig. 5 (b). The large amplitude of the induced component in the p_- -wave domain is the origin of the different behavior of the vortex structure between the p_+ -wave domain and the p_- -wave domain cases.

The magnetic field dependence of the internal field distribution is shown in Fig. 6. There, we plot H -dependence of the maximum h_{\max} and the minimum h_{\min} of $h(\mathbf{r})$. The p_+ -wave case and the s -wave pairing case have similar internal field distributions. h_{\max} is the internal field at the vortex center. Compared with the

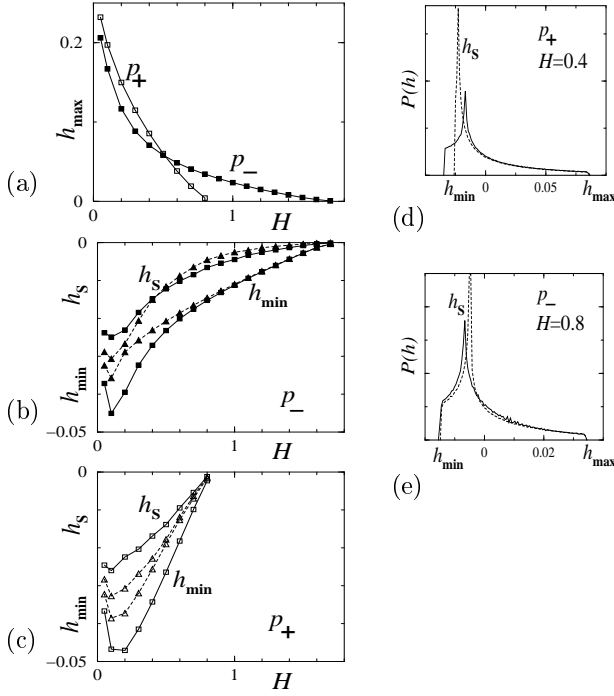


FIG. 6: Field dependence of the internal field distribution. (a) Internal field at the vortex center, h_{\max} , in the p_- -wave and the p_+ -wave domain cases. Both the square and the triangular lattice configurations give same h_{\max} . (b) The minimum h_{\min} of the internal field, and the peak field h_s of the distribution function $P(h)$ in the p_- -wave domain case. Solid (dashed) lines are for the square (triangular) vortex lattice configuration. (c) The same as (b), but in the p_+ -wave domain case. (d) Internal field distribution function $P(h)$ at $H = 0.4$ in the p_+ -wave domain case. Solid (dashed) lines are for the square (triangular) vortex lattice configuration. (e) The same as (d), but at $H = 0.8$ in the p_- -wave domain case.

p_- -wave domain case, h_{\max} in the p_+ -wave domain case is larger at low H , and becomes smaller at higher H , because $h_{\max} \rightarrow 0$ with approaching low H_{c2} . We obtain same h_{\max} both in the square and the triangular vortex lattice configurations.

The internal field distribution function is defined as

$$P(h) = \langle \delta(h - h(\mathbf{r})) \rangle_{\mathbf{r}} \quad (15)$$

with the δ -function. We can observe $P(h)$ as the resonance line shape in the NMR or μ SR experiments. Figure 6(d) shows $P(h)$ at $H = 0.4$ in the p_+ -wave domain case. It is a typical distribution shape as in the conventional superconductor, i.e., h_{\min} is the internal field at the C-point on the unit cell boundary, and peak field h_s corresponds to the internal field at the saddle point S.⁴⁴ The vortex lattice configuration affects the distance between h_s and h_{\min} . Compared with the square lattice configuration, $h_s - h_{\min}$ is small in the triangular lattice configuration. Figure 6(c) shows that this property of $P(h)$ appears for all H region in the p_+ -wave domain case.

Figure 6(e) shows $P(h)$ at $H = 0.8$ in the p_- -wave domain case, which gives anomalous distribution of $h(\mathbf{r})$

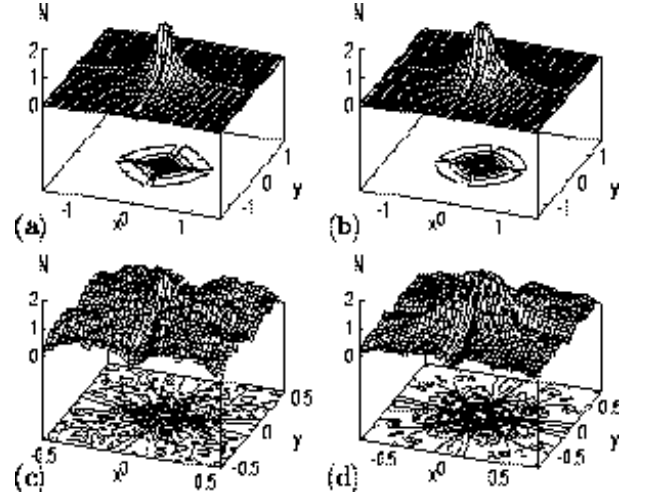


FIG. 7: Zero-energy local density of states in the p_- -wave domain case at $H = 0.1$ (a), 0.8 (c), and in the p_+ -wave domain case at $H = 0.1$ (b), 0.4 (d). We plot $N(E = 0, \mathbf{r})/N_0$ within a unit cell. The peak at the vortex center is truncated at $N(E = 0, \mathbf{r})/N_0 = 2$ to show the tail structure extending from the vortex core.

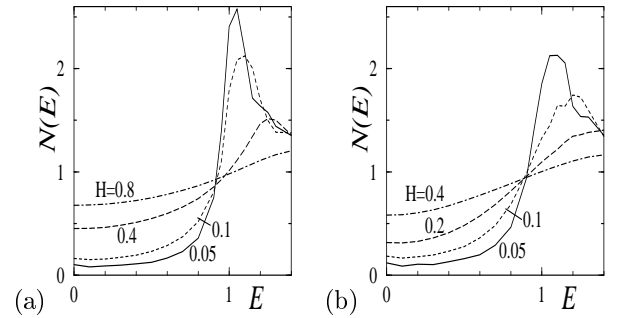


FIG. 8: Spectrum of the spatially averaged DOS, $N(E)/N_0$. (a) In the p_- -wave domain case at $H = 0.05, 0.1, 0.4, 0.8$. (b) In the p_+ -wave domain case at $H = 0.05, 0.1, 0.2, 0.4$. The square and the triangular vortex lattice configurations give same result. The spectrum of the p_+ -wave domain case is almost the same as in the s -wave pairing case.

at the unit cell boundary, as shown in Figs. 2(b) and 4(d). There, the position giving h_{\min} (h_s) shifts to other position than the C- (S-) point on the boundary. In this distribution, the square and the triangular lattice configurations give similar $P(h)$ distribution. When we see the field dependence of h_s and h_{\min} in Fig. 6(b), there is a small difference between the triangular and the square lattice configurations at higher field $H > 0.4$. But, at lower field $H < 0.4$, there appears eminent difference in the distance between h_s and h_{\min} for the two vortex lattice configurations. There $P(h)$ has similar distribution as in Fig. 6(d). It is interesting that the square vortex lattice configuration has lower free energy than the triangular one in the field region $H > 0.4$, showing anomalous field distribution.

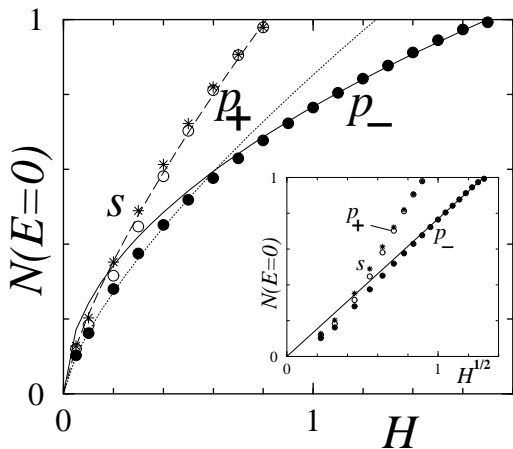


FIG. 9: Field dependence of the zero-energy DOS $N(0)/N_0$ in the p_- -wave domain case (\bullet), the p_+ -wave domain case (\circ), and the s -wave case ($*$). Points show numerical data, and lines are fitting curves by $N(0) \propto H^\alpha$. Dashed line and dotted line are for $\alpha=0.74$ and 0.71 , respectively. Solid line is for $N(0) \propto \sqrt{H}$. Inset: $N(0)/N_0$ is plotted as a function of \sqrt{H} . The solid line shows the relation $N(0) \propto \sqrt{H}$.

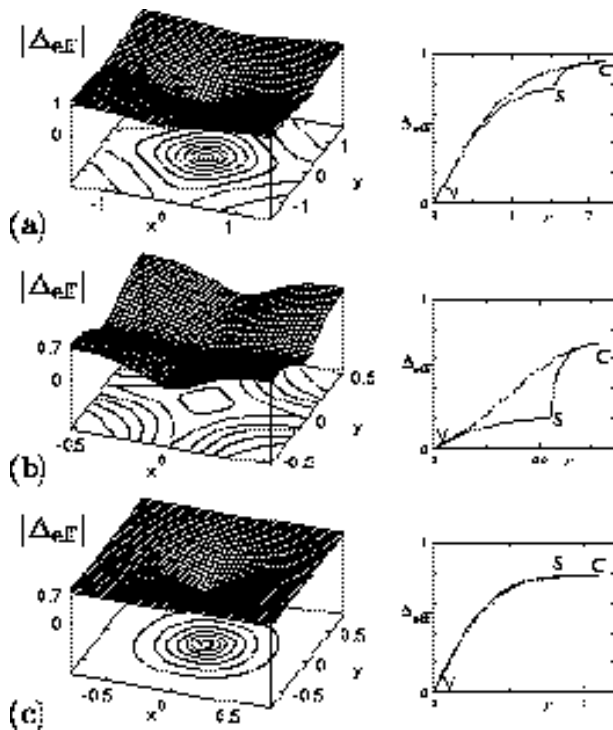


FIG. 10: Effective pair potential for zero-energy quasiparticles. We plot $|\Delta_{\text{eff}}(\mathbf{r})| = |\Delta(\theta_{\mathbf{r}}, \mathbf{r})|$ at low field $H = 0.1$ (a) and at higher field $H = 0.8$ (b) in the p_- -wave domain case, and at $H = 0.4$ in the p_+ -wave domain case (c). The left panels are the stereographic view within a unit cell region. There is a vortex at the center of the figures. The right panels are the profiles along the path presented in Fig. 3(a).

V. QUASIPARTICLE STRUCTURE IN THE VORTEX STATE

The LDOS is expected to be observed by the scanning tunneling microscopy (STM), which will experimentally give the detailed information of the quasiparticle structure around vortices. We study the LDOS at zero energy, which dominantly contributes to the low temperature behaviors. Figures 7 (a) and (b) show $N(E=0, \mathbf{r})$ at low field $H = 0.1$ in the p_- -wave and the p_+ -wave domain cases, respectively. Since the gap function has full gap as in the s -wave pairing, the low energy states are localized at the vortex core. We see that the localized LDOS is slightly suppressed along the NN and NNN vortex directions. It is the effect of the inter-vortex transfer of the low energy quasiparticles.^{15,16,17,18,39}

Higher field case at $H \sim 0.5H_{c2}$ are presented in Fig. 7 (c) and (d). Figure 7 (c) is for the p_- -wave domain case at $H = 0.8$, and Fig. 7 (d) is for the p_+ -wave domain case at $H = 0.4$. Since the inter-vortex distance becomes short at high field, the LDOS localized at vortex cores are overlapped each other. We see the eminent suppression along the NN and NNN vortex directions due to the inter-vortex transfer. The localized LDOS around the vortex core is reduced to uniform distribution when approaching H_{c2} . Then, the sharp peak at the vortex center survives until higher field in the p_- -domain case, since it has higher H_{c2} .

The spectrum of the spatially averaged DOS, $N(E)$, is presented in Fig. 8. The full gap structure for $E < \Delta_0$ and the peak of the gap edge at $E = \Delta_0$ are gradually smeared by low energy quasiparticles around the vortex. These behaviors of the LDOS and spectrum $N(E)$ are the same as in the isotropic s -wave case previously reported.^{15,16,17,18} When we see the spatial structure of the LDOS, we do not find drastic changes by the chirality effect. We see qualitatively the same structure both for the p_- -wave domain and p_+ -wave domain cases.

However, when we consider the quantitative field dependence of the DOS $N(0)$ by spatially averaging the LDOS at $E = 0$, we can see the characteristic behavior of the chiral p -wave pairing. Figure 9 shows the field dependence of $N(0)$. Numerical data are presented by points, and lines are fitting curves by the relation $N(0) \propto H^\alpha$. The square and the triangular vortex lattice configurations give the same result.

In the p_+ -wave domain case, $N(0)$ shows similar behavior as that of the s -wave pairing case. But $N(0)$ is slightly smaller than that of the s -wave case at low field. Fitting curve is given by $\alpha = 0.74$ in the s -wave case for $\kappa = 2.7$. In the p_- -wave domain case, lower field data are fitted by $\alpha = 0.71$. But, higher field data are fitted by $\alpha = 0.5$. To see the \sqrt{H} -behavior, we plot $N(0)$ as a function of \sqrt{H} in the inset. At higher field, $N(0)$ is on the line $N(0) \propto \sqrt{H}$. This \sqrt{H} -behavior at higher field is qualitatively consistent with the experimental data of the specific heat.³⁰ We note that this \sqrt{H} is not the so-called Volovik effect for the vertical line node of the $k_x^2 - k_y^2$

type.^{15,22} In the vertical line node case, the \sqrt{H} -behavior appears from low field. According to the recent directional dependent thermal-conductivity experiment under parallel field,⁴⁵ there is no in-plane gap anisotropy, implying the absence of the vertical line node.

Unless we consider the induced component of the pair potential, $|\Delta(\theta, \mathbf{r})| = |\Delta_-(\mathbf{r})\phi_-(\theta)|$ gives full gap, as in the s -wave pairing case. Then, we can not expect the \sqrt{H} -behavior of $N(0)$. However, when we take account of the induced component, $|\Delta(\theta, \mathbf{r})| = |\Delta_-(\mathbf{r})\phi_-(\theta) + \Delta_+(\mathbf{r})\phi_+(\theta)|$ can be small for particular direction θ , if the induced component $|\Delta_+(\mathbf{r})|$ is large. To discuss the origin of the \sqrt{H} -behavior at higher field, we consider the effective pair potential for zero-energy quasiparticles. When we analyze the LDOS at $E = 0$, the main contribution comes from the quasiparticle trajectory passing through the vortex center (i.e., line with the impact parameter $r_\perp = 0$),³⁹ since zero-energy quasiparticles are localized around the vortex core. Then, the zero-energy LDOS at $\mathbf{r} = (x, y)$ dominantly consists of quasiparticles traveling along the quasiparticle trajectory with the direction $\theta_{\mathbf{r}} = \tan^{-1}(y/x)$. They feel the effective pair potential $\Delta_{\text{eff}}(\mathbf{r}) \equiv \Delta(\theta_{\mathbf{r}}, \mathbf{r}) = \Delta_+(\mathbf{r})\phi_+(\theta_{\mathbf{r}}) + \Delta_-(\mathbf{r})\phi_-(\theta_{\mathbf{r}})$.

Figure 10 shows amplitude $|\Delta_{\text{eff}}(\mathbf{r})|$ for some typical cases. In the p_- -wave domain case, $|\Delta_{\text{eff}}(\mathbf{r})| \sim |\Delta_-(\mathbf{r})| - |\Delta_+(\mathbf{r})|$, i.e., the induced component $|\Delta_+(\mathbf{r})|$ suppresses the effective pair potential. At low field, since the induced component is localized around the vortex core, $|\Delta_{\text{eff}}(\mathbf{r})|$ is suppressed around the vortex core as shown in Fig. 10(a). Since the amplitude of the effective pair potential is still large at the boundary of the unit cell, we expect the bound quasiparticle states around the vortex core. Then, the exponent $\alpha \sim 0.71$ is not largely different from that of the s -wave case. At higher H , the ratio of the induced component is enhanced, and $|\Delta_+(\mathbf{r})|$ has large amplitude at the boundary of the unit cell. Since the induced component $|\Delta_+(\mathbf{r})|$ is large in the NN vortex direction [Fig. 2(b)], $|\Delta_{\text{eff}}(\mathbf{r})|$ is largely suppressed in this direction, as shown by line VS in Fig. 10(b). The effective pair potential is not suppressed at the C-points, since there is no induced component there. Also in the triangular vortex lattice configuration, $|\Delta_{\text{eff}}(\mathbf{r})|$ gives the similar structure. There, $|\Delta_{\text{eff}}(\mathbf{r})|$ is eminently suppressed along six NN vortex directions. With increasing H , $|\Delta_{\text{eff}}(\mathbf{r})|$ along the NN direction is more suppressed, since the ratio $\Delta_+^{\text{max}}/\Delta_-^{\text{max}}$ increases monotonically. Then, the low energy quasiparticles can easily transfer between NN vortices at higher field. When low energy quasiparticles are extended to the boundary of the unit cell as in the d -wave pairing case, we expect the \sqrt{H} -like behavior.^{15,22} It is the origin of the relation $N(0) \sim \sqrt{H}$ at high field.

On the other hand, in the p_+ -wave domain case, $|\Delta_{\text{eff}}(\mathbf{r})| \sim |\Delta_+(\mathbf{r})| + |\Delta_-(\mathbf{r})|$, i.e., the induced component $|\Delta_-(\mathbf{r})|$ enhances the effective pair potential, as shown in Fig. 10(c). Then, low energy quasiparticles are bound states, as in the s -wave pairing case in all H range. Due to the enhancement of the effective pair potential by

the induced component, $N(0)$ is slightly suppressed than that of the s -wave case. With approaching H_{c2} , $N(0)$ is reduced the s -wave case's value, since the induced component is decreased to zero.

VI. SUMMARY AND DISCUSSIONS

We have investigated the field dependence of the vortex structure in chiral p -wave superconductors. We have shown the difference of the vortex structure for the p_+ -wave domain case and the p_- -wave domain case. The difference comes from the structure of the induced opposite chiral component. When we compare the free energy, the p_- -wave domain is the stable state, and the p_+ -wave domain is metastable. Then, the transition of the p_+ -wave domain to the p_- -wave domain may occur. We expect different vortex lattice configuration for the domains, i.e., square-like lattice in the p_- -wave domain and triangular lattice in the p_+ -wave domain.

The phase winding structure of the induced component of the pair potential is different depending on the chirality. In the p_+ -wave domain, the amplitude of the induced component is small and reduced to zero near H_{c2} . Then, the vortex structure is similar to that of the isotropic s -wave pairing case. And H_{c2} is same as in the s -wave pairing case in the two-dimensional Fermi surface. In the p_- -wave domain case, the opposite chiral component is largely induced. Then, the superconductivity can survive until high field, giving high H_{c2} . The induced component produces the characteristic vortex structure in the chiral p -wave superconductors, such as an anomalous internal field distribution.

The LDOS structure shows that low energy quasiparticles are bound states around the vortex core, and there are some inter-vortex transfers. At higher field, the bound states are overlapped between neighbor vortices. When we quantitatively consider the field dependence of the zero energy DOS $N(0) \propto H^\alpha$, we obtain the effect of the chiral p -wave superconductivity. The stable p_- -wave domain case shows \sqrt{H} -behavior at higher field. It is because the effective pair potential for zero energy quasiparticles are suppressed along the NN vortex direction by the induced opposite chiral component of the pair potential. At low field, the suppression by the induced component is restricted in the vortex core region, the low energy quasiparticles are still bound around the vortex core. Then the exponent α is near the value for the s -wave pairing at low field.

The superconducting state in Sr_2RuO_4 is suggested to be the chiral p -wave pairing. If we can experimentally observe the domain structure of the p_+ -wave and the p_- -wave pairing regions, it becomes firm evidence for the chiral p -wave superconductivity. In this observation, the information of the vortex structure difference for the p_\pm -wave domains is helpful to analyze the chirality p_\pm of each domain. For example, the internal field distribution and the stable vortex lattice configuration

may be different depending on the chirality of the domain. The specific heat measurement on Sr_2RuO_4 reports that $N(0) \propto \sqrt{H}$ at high field, while it deviates from \sqrt{H} at low field.³⁰ It is qualitatively consistent with our results. However, when we analyze the experimental data on Sr_2RuO_4 , there are some factors to quantitatively modify our results on a simple isotropic system, such as the possibility of the line node along the basal plane direction, the orbital dependence and anisotropy of the Fermi surface and the gap functions.^{31,32,33,34,35,36,37} The study on these additional effects remains in future problems.

Acknowledgments

We would like to thank N. Hayashi, M. Takigawa, N. Nakai, P. Miranovic and M. Sigrist for their helpful comments and discussions.

APPENDIX A: SYMMETRY RELATION

When one of the vortex center locates at $\mathbf{r} = 0$, there is a relation $\Delta(\theta, \mathbf{r}) = -\Delta(\theta, -\mathbf{r})$. Then, considering the transformation $\mathbf{r} \rightarrow -\mathbf{r}$ in the Eilenberger equations (1)-(3), we obtain the following relations of the quasiclassical Green's functions,

$$\begin{aligned} f(\omega_n, \theta, -\mathbf{r}) &= -f^{\dagger*}(\omega_n^*, \theta, \mathbf{r}), \\ f^\dagger(\omega_n, \theta, -\mathbf{r}) &= -f^*(\omega_n^*, \theta, \mathbf{r}), \\ g(\omega_n, \theta, -\mathbf{r}) &= g^*(\omega_n^*, \theta, \mathbf{r}). \end{aligned} \quad (\text{A1})$$

Then, in the calculation of the Matsubara frequency ω_n or $E = 0$, it is enough to solve the Eilenberger equations in half area of a unit cell.

When the vortex lattice is symmetric under the reflection at the x axis, i.e., $S\mathbf{r} = (x, -y)$, there is a relation $\Delta(-\theta, S\mathbf{r}) = -e^{i\alpha}\Delta^*(\theta, \mathbf{r})$. The factor $e^{i\alpha}$ comes from

$\phi(-\theta) = e^{i\alpha}\phi^*(\theta)$ for the pairing function of the dominant component of the pair potential. Then, considering the transformation $S\mathbf{r}$ and $\theta \rightarrow -\theta$ in Eqs. (1)-(3), we obtain the following relations of the quasiclassical Green's functions,

$$\begin{aligned} f(\omega_n, -\theta, S\mathbf{r}) &= -e^{i\alpha}f^*(\omega_n, \theta, \mathbf{r}), \\ f^\dagger(\omega_n, -\theta, S\mathbf{r}) &= -e^{-i\alpha}f^{\dagger*}(\omega_n, \theta, \mathbf{r}), \\ g(\omega_n, -\theta, S\mathbf{r}) &= g^*(\omega_n, \theta, \mathbf{r}). \end{aligned} \quad (\text{A2})$$

Next, we consider the ψ -rotation around the vortex center at $\mathbf{r} = 0$, i.e., $R_\psi\mathbf{r} = (x \cos \psi - y \sin \psi, x \sin \psi + y \cos \psi)$. Generally, vortex lattice has the symmetry for the rotation $\psi = \pi$. And further, the square (triangular) vortex lattice has the symmetry for the rotation $\psi = \pi/2$ ($\psi = \pi/3$). Under these rotations, $\Delta(\theta + \psi, R_\psi\mathbf{r}) = e^{i(\alpha' - \psi)}\Delta(\theta, \mathbf{r})$ in the symmetric gauge. The factor $e^{i\alpha'}$ comes from $\phi(\theta + \psi) = e^{i\alpha'}\phi(\theta)$. Then, considering the translation $R_\psi\mathbf{r}$ and $\theta \rightarrow \theta + \psi$ in Eqs. (1)-(3), we obtain

$$\begin{aligned} f(\omega_n, \theta + \psi, R_\psi\mathbf{r}) &= e^{i(\alpha' - \psi)}f(\omega_n, \theta, \mathbf{r}), \\ f^\dagger(\omega_n, \theta + \psi, R_\psi\mathbf{r}) &= e^{-i(\alpha' - \psi)}f^\dagger(\omega_n, \theta, \mathbf{r}), \\ g(\omega_n, \theta + \psi, R_\psi\mathbf{r}) &= g(\omega_n, \theta, \mathbf{r}). \end{aligned} \quad (\text{A3})$$

In the pair potential $\Delta(\theta, \mathbf{r}) = \Delta_-(\mathbf{r})\phi_-(\theta) + \Delta_+(\mathbf{r})\phi_+(\theta)$, the pairing function $\phi_\pm(\theta)$ of the induced component may produce different phase factor from that of the dominant component $\phi_\mp(\theta)$ in the transformation $\phi(\theta + \psi) = e^{i\alpha'}\phi(\theta)$. Then, the phase of the induced component $\Delta_\pm(\mathbf{r})$ should be changed so as to cancel the difference of the phase factors in the rotational transformation. This is the origin of the different phase winding of the induced component in Figs. 3 and 4.

Using these symmetry relations, it is enough to solve the Eilenberger equations (1)-(3) for $0 \leq \theta < \pi/4$ ($0 \leq \theta < \pi/6$) in the square (triangular) vortex lattice configuration.

* Electronic address: oka@mp.okayama-u.ac.jp

† Electronic address: machida@mp.okayama-u.ac.jp

¹ Y. Maeno, H. Hashimoto, K. Yoshida, S. Nishizaki, T. Fujita, J.G. Bednorz, and F. Lichtenberg, *Nature* **372**, 532 (1994).

² T.M. Rice and M. Sigrist, *J. Phys.: Cond. Matter* **7**, L643 (1995).

³ K. Ishida, H. Mukuda, Y. Kitaoka, K. Asayama, Z.Q. Mao, Y. Mori, and Y. Maeno, *Nature* **396**, 658 (1998).

⁴ G.M. Luke, Y. Fudamoto, K.M. Kojima, M.I. Larkin, J. Merrin, B. Nachumi, Y.J. Uemura, Y. Maeno, Z.Q. Mao, Y. Mori, H. Nakamura, and M. Sigrist, *Nature* **394**, 558 (1998).

⁵ R. Heeb and D.F. Agterberg, *Phys. Rev. B* **59**, 7076 (1999).

⁶ R. Heeb, Doctor thesis, ETH Zürich (2000).

⁷ Y. Kato, *J. Phys. Soc. Jpn.* **69**, 3378 (2000).

⁸ Y. Kato and N. Hayashi, *J. Phys. Soc. Jpn.* **70**, 3368 (2001).

⁹ M. Matsumoto and M. Sigrist, *J. Phys. Soc. Jpn.* **68**, 724 (1999).

¹⁰ M. Matsumoto and R. Heeb, *Phys. Rev. B* **65**, 014504 (2002).

¹¹ M. Takigawa, M. Ichioka, K. Machida, and M. Sigrist, *Phys. Rev. B* **65**, 014508 (2002).

¹² K. Scharnberg and R.A. Klemm, *Phys. Rev. B* **22** (1980) 5233.

¹³ K. Scharnberg and R.A. Klemm, *Phys. Rev. Lett.* **54** (1985) 2445.

¹⁴ G. Eilenberger, *Z. Phys.* **214**, 195 (1968).

¹⁵ M. Ichioka, A. Hasegawa, and K. Machida, *Phys. Rev. B* **59**, 184 (1999).

- ¹⁶ M. Ichioka, A. Hasegawa, and K. Machida, *Phys. Rev. B* **59**, 8902 (1999).
- ¹⁷ M. Ichioka, A. Hasegawa, and K. Machida, *J. Superconductivity* **12**, 571 (1999).
- ¹⁸ M. Ichioka, N. Hayashi, and K. Machida, *Phys. Rev. B* **55**, 6565 (1997).
- ¹⁹ M. Ichioka, N. Hayashi, N. Enomoto, and K. Machida, *Phys. Rev. B* **53**, 15316 (1996).
- ²⁰ M. Ichioka, N. Enomoto, N. Hayashi, and K. Machida, *Phys. Rev. B* **53**, 2233 (1996).
- ²¹ T. Akima, S. NishiZaki, and Y. Maeno, *J. Phys. Soc. Jpn.* **68**, 694 (1999).
- ²² G.E. Volovik, *JETP Lett.* **58**, 469 (1993).
- ²³ K.A. Moler, D.J. Baar, J.S. Urbach, R. Liang, W.N. Hardy, and A. Kapitulnik, *Phys. Rev. Lett.* **73**, 2744 (1994).
- ²⁴ R.A. Fisher, J.E. Gordon, S.F. Reklis, D.A. Wright, J.P. Emerson, B.F. Woodfield, E.M. McCarron III, and N.E. Phillips, *Physica C* **252**, 237 (1995).
- ²⁵ A.P. Ramirez, *Phys. Lett. A* **211**, 59 (1996).
- ²⁶ M. Hedo, Y. Inada, E. Yamamoto, Y. Haga, Y. Ōnuki, Y. Aoki, T.D. Matsuda, H. Sato, and S. Takahashi, *J. Phys. Soc. Jpn.* **67**, 272 (1998).
- ²⁷ A.A. Golubov and U. Hartmann, *Phys. Rev. Lett.* **72**, 3602 (1994).
- ²⁸ J.E. Sonier, R.F. Kiefl, J.H. Brewer, J. Chakhalian, S.R. Dunsiger, W.A. MacFarlane, R.I. Miller, A. Wong, G.M. Luke, and J.W. Brill, *Phys. Rev. Lett.* **79**, 1742 (1997).
- ²⁹ J.E. Sonier, J.H. Brewer, and R.F. Kiefl, *Rev. Mod. Phys.* **72**, 769 (2000).
- ³⁰ K. Deguchi and Y. Maeno, private communication.
- ³¹ K. Machida, M. Ozaki, and T. Ohmi, *J. Phys. Soc. Jpn.* **65**, 3720 (1996).
- ³² M. Sigrist and M.E. Zhitomirsky, *J. Phys. Soc. Jpn.* **65**, 3452 (1996).
- ³³ Y. Hasegawa, K. Machida, and M. Ozaki, *J. Phys. Soc. Jpn.* **69**, 336 (2000).
- ³⁴ M.J. Graf and A.V. Balatsky, *Phys. Rev. B* **62**, 9697 (2000).
- ³⁵ M.E. Zhitomirsky and T.M. Rice, *Phys. Rev. Lett.* **87**, 057001 (2001).
- ³⁶ K.K. Ng and M. Sigrist, *Europhys. Lett.* **49**, 473 (2000).
- ³⁷ K. Miyake and O. Narikiyo, *Phys. Rev. Lett.* **83**, 1423 (1999).
- ³⁸ U. Klein, *J. Low Temp. Phys.* **69**, 1 (1987).
- ³⁹ U. Klein, *Phys. Rev. B* **40**, 6601 (1989).
- ⁴⁰ B. Pöttinger and U. Klein, *Phys. Rev. Lett.* **70**, 2806 (1993).
- ⁴¹ D.F. Agterberg, *Phys. Rev. Lett.* **80**, 5184 (1998).
- ⁴² T. Kita, *Phys. Rev. Lett.* **83**, 1846 (1999).
- ⁴³ T.M. Riseman, P.G. Kealy, E.M. Forgan, A.P. Mackenzie, L.M. Galvin, A.W. Tyler, S.L. Lee, C. Ager, D.McK. Paul, C.M. Aegerter, R. Cubitt, Z.Q. Mao, S. Akima, and Y. Maeno, *Nature* **396**, 242 (1998).
- ⁴⁴ A.L. Fetter and P.C. Hohenberg, in *Superconductivity*, ed. R.D. Parks (Marcel Dekker, New York, 1969), p.841.
- ⁴⁵ K. Izawa, H. Takahashi, H. Yamaguchi, Y. Matsuda, M. Suzuki, T. Sasaki, T. Fukase, Y. Yoshida, R. Settai, Y. Ōnuki, *Phys. Rev. Lett.* **86**, 2653 (2001).